

Evidence of charge transfer in three-dimensional topological insulator/antiferromagnetic Mott insulator $\text{Bi}_1\text{Sb}_1\text{Te}_{1.5}\text{Se}_{1.5}/\alpha\text{-RuCl}_3$ heterostructures

Shoubhik Mandal , Debarghya Mallick, Abhishek Banerjee, R. Ganesan , and P. S. Anil Kumar 
Department of Physics, Indian Institute of Science, Bengaluru-560012, India



(Received 29 December 2022; revised 6 May 2023; accepted 8 May 2023; published 14 June 2023)

We report magnetotransport measurements on $\text{Bi}_1\text{Sb}_1\text{Te}_{1.5}\text{Se}_{1.5}/\text{RuCl}_3$ heterostructure nanodevices. $\text{Bi}_1\text{Sb}_1\text{Te}_{1.5}\text{Se}_{1.5}$ (BSTS) is a strong three-dimensional topological insulator (3D-TI) that hosts conducting topological surface states (TSS) enclosing an insulating bulk. $\alpha\text{-RuCl}_3$ (namely, RuCl_3) is an antiferromagnet that is predicted to behave as a Kitaev-like quantum spin liquid carrying chargeless Majorana excitations. Temperature (T)-dependent resistivity measurements on BSTS show the interplay between parallel bulk and surface transport channels. For $T < 150$ K, surface state transport dominates over bulk transport. Multichannel weak antilocalization (WAL) is observed as a sharp cusp in the low-field magnetoconductivity, indicating strong spin-orbit coupling. The presence of top and bottom topological surface states (TSS) including a pair of electrically coupled Rashba surface states (RSS) is indicated. The nonlinear Hall effect, explained by a two-band model, further supports this interpretation. We observed that RuCl_3 has an electrostatic effect on the TSS of BSTS, that is, it changes bandbending at the interface as a result of charge transfer. In this regard, the change in low- T logarithmic resistivity upturn in the presence of out-of-plane magnetic field is analyzed employing the Lu-Shen model, supporting the presence of gapless surface states (TSS and RSS) with a π Berry phase.

DOI: [10.1103/PhysRevB.107.245418](https://doi.org/10.1103/PhysRevB.107.245418)

I. INTRODUCTION

Topological surface states (TSS) on a three-dimensional (3D) topological insulator (TI) harbors massless Dirac fermions [1–5]. A combination of large spin-orbit interaction and time reversal symmetry determines the properties of TSS, including suppression of backscattering featured in spin-momentum locking and weak antilocalization (WAL) effect. So, TIs have attracted great attention as a candidate for dissipationless spintronics applications and quantum computation. The chalcogenide material (Bi, Sb, Te, Se) based quaternary TIs such as $\text{Bi}_1\text{Sb}_1\text{Te}_{1.5}\text{Se}_{1.5}$ (BSTS) exhibits the gapless surface spectrum in the insulating bulk even at room temperatures, and bulk resistivity increases by several orders at low temperatures, thus opening the route to access TSS [2,6–12]. In addition, BSTS hosts Rashba spin-split states originating from quantum confined bulk carriers forming two-dimensional electron gas (2DEG), namely Rashba surface states (RSS) with gapless spectrum carrying π Berry phase, similar to TSS [13].

On the other hand, $\alpha\text{-RuCl}_3$, an antiferromagnet, is known as a proximate Kitaev spin liquid candidate [14–16] and a Mott-Hubbard insulator with a band gap of 1.1 eV induced by a strong electron-electron correlation [17,18], and the transport gap of 0.3 eV, calculated from temperature-dependent resistivity measurements [19]. Moreover, the neutron scattering experiment [20], half-integer thermal Hall effect measurement [21–23], and optical studies prove the presence of physical Majorana fermions [24] which could not be detected in electrical transport. In contrast, the TI-superconductor junction also hosts Majorana fermions which are electrically accessible [1].

However, due to very high resistance, the electrical transport of $\alpha\text{-RuCl}_3$ is challenging. Recently, it has been theoretically proposed that the interfacial layer of $\alpha\text{-RuCl}_3$ can inject excess holes into the proximitized material due to strain and the difference in work functions of two neighboring materials [25]. Recently, the charge transfer is realized in the electrical transport of the graphene (monolayer)/ $\alpha\text{-RuCl}_3$ device [26,27] as a signature of splitting in the frequency of Shubnikov de-Haas oscillations, supporting the creation of an additional hole band. Furthermore, the small nonzero net magnetic moment of $\alpha\text{-RuCl}_3$ induces a magnetic proximity effect on monolayer graphene as observed in the electrical transport even though $\alpha\text{-RuCl}_3$ is “weak” to show magnetic proximity effect in comparison to other ferromagnetic insulators (for example, Garnets, EuS etc.). The charge transfer properties of $\alpha\text{-RuCl}_3$ have been further manipulated to obtain nanometer-scale p-n junction on a monolayer graphene [28]. The use of $\alpha\text{-RuCl}_3$ as a passive charge transfer interface and the tunable electrostatic gate is expanded in transition metal dichalcogenides/ $\alpha\text{-RuCl}_3$ heterostructure [29,30]. Therefore, $\alpha\text{-RuCl}_3$ is “special” in comparison to other kinds of insulators such as hexagonal Boron nitride (hBN) which show no charge transfer effect based upon the observations reported in various literatures. However, the charge transfer doping on a TI has yet to be explored. These facts motivated us to fabricate the device out of BSTS/ RuCl_3 heterostructure.

In this work, we discuss the results of the electronic transport of 3D TI $\text{Bi}_1\text{Sb}_1\text{Te}_{1.5}\text{Se}_{1.5}$ (BSTS) in proximity to Mott insulator RuCl_3 by fabricating heterostructure nanodevices of various thicknesses of the TI and RuCl_3 flakes. We carried out low-temperature magnetotransport measurements in the presence of out-of-plane magnetic field ($B \parallel c$) to probe the

proximity effect on the metallic surface states in TI. The analysis of WAL featured in magnetoconductance and the nonlinear Hall effect yield the affirmative presence of multiple conducting coherent spin-orbit coupled channels, including top and bottom TSS and RSS [31,32]. Linear Logarithmic temperature-dependent conductance in the low-temperature regime suggests the presence of electron-electron interaction and quantum interference effects in our system and we extracted the linear slope based on the Lu-Shen model [33]. On applying out-of-plane magnetic field, the slope quickly saturates to a constant value, indicating the vanishing quantum interference effect. Furthermore, we extracted the maximum change of slope from the temperature-dependent conductance curves at various constant magnetic fields and probed the nature and number of gapless surface states. Our comprehensive analysis suggests a certain thickness threshold of RuCl₃ layer for the effective charge transfer to occur at the TI-RuCl₃ interface. In this regard, we present the theory of band bending combined with the Lu-Shen formalism to probe gapless surface states.

II. SAMPLE GROWTH AND DEVICE FABRICATION

We have synthesized the high-quality single crystals of Bi₁Sb₁Te_{1.5}Se_{1.5} via the modified Bridgman method in a high-temperature vertical furnace. We utilized x-ray diffraction (XRD) methods to characterize the single-crystalline nature of as-grown crystals. XRD patterns recorded by shining Cu K_α x-ray show the growth along (0, 0, L) directions (see the Supplemental Material [34]). Further, an electron probe microanalyzer (EPMA) was employed to determine the stoichiometry of the crystal. On the other hand, black lustrous RuCl₃ crystals are grown using the physical vapor transport technique in a horizontal dual-zone furnace (750 °C at the hot end and 650 °C at the cold end). Similarly, XRD and EPMA studies helped to prove the growth of high-quality single crystals (see the Supplemental Material [34]). We fabricated the Bi₁Sb₁Te_{1.5}Se_{1.5}/RuCl₃ heterostructure by hot and dry transfer technique inside an Argon-filled and water-vapor free glove box with O₂ < 0.1 ppm (see the Supplemental Material [34]).

The thicknesses of BSTS and RuCl₃ flakes were measured using atomic force microscopy. The electrical contacts forming the Hall bar pattern were made by e-beam lithography following Cr(10 nm)/Au(200 nm) deposition. Prior to the transport measurement carried out in cryostat (Oxford Instruments, UK), the devices were packaged inside a chip carrier and wirebonded.

III. RESULTS AND DISCUSSION

A. Zero-field electrical transport

Figure 1(c) shows an increase in sheet resistance (R_{\square}) with lowering the temperature and turning it into metal below $T \approx 150$ K. The sheet resistance is calculated by the formula $R_{\square} = R(\frac{W}{L})$, where R is the sample resistance, and W and L denote the channel width and length, respectively (see the Supplemental Material [34]). The metallic conduction suggests the surfacstates dominated transport for $T < 150$ K, whereas the bulk charge carriers cause insulating behavior at high temperatures ($T > 150$ K).

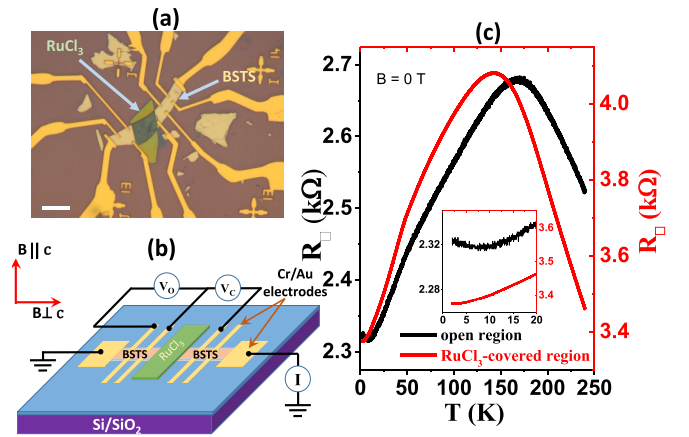


FIG. 1. Zero-field electrical transport. (a) A typical Bi₁Sb₁Te_{1.5}Se_{1.5} (BSTS)/RuCl₃ heterostructure device. The Cr/Au electrodes are fabricated on BSTS only. Scalebar indicates the length of 10 μm . (b) The device schematic with magnetic field configurations. V_0 and V_c are the voltages measured for the pair of probes placed on the open region and across RuCl₃ covered region, respectively. (c) Temperature-dependent longitudinal sheet resistance for the open (black) and RuCl₃-covered (red) regions for the BSTS(105 nm)/RuCl₃(20 nm) heterostructure device (D4). High-temperature insulator to low-temperature metallic transition occurs at approximately 150 K. Inset shows the low temperature sheet resistance upturn.

As our interest lies in the proximity effect of RuCl₃ on BSTS, we divided all possible successive pairs of voltage probes into two types: (1) one pair of probes rest upon the open surface of the BSTS flake and (2) another pair across the RuCl₃-covered region, as depicted in the Figs. 1(a) and 1(b). We have measured resistances using both pairs of probes to make a comparative study.

1. Conduction due to surface states

To extract the surface contribution to resistance, one may use a parallel bulk-surface channel transport model, where the total conductance is the sum of the surface and the bulk conductance. Here we assume that the resistance $R_{\square}(T)$ of the metallic surface states follows a linearly decreasing trend until 25 K. At very low temperatures, electron-electron interaction (EEI) also contributes to the resistance, deviating from linear temperature-dependency to power-law one. Below 25 K, the resistance has T^2 -dependence, indicating the presence of electron-electron scattering with large momentum transfer, characteristic of Fermi liquid (see the Supplemental Material [34]).

Below 10 K, we notice an upturn in the sheet resistance instead of saturation generally observed in a disordered metal while approaching 0 K. There are ongoing debates on the origin of the resistance upturn, extensively observed in the case of TI [35–40]. The possible cause is proposed to be due to Anderson localization induced by strong electron-electron scattering in the presence of disorders [33]. There is a clear contrast in the slope of the upturn for both regions of the BSTS flake. The resistance measured on the open region shows an upturn steeper than in the case of the RuCl₃-covered region.

Though the origin of the upturn is not clear to date, the effect of the magnetic field has great importance in the study of surface states in TI [33].

In order to formulate the upturn, we plotted the 2D conductance G_S vs $\ln T$ and found $G_S \sim \ln T$ in the range $3 \text{ K} < T < 10 \text{ K}$ (Figs. 4 and 5). This $\ln T$ dependence of the 2D conductance is suggested to be due to EEI for conventional electrons. However, an additional mechanism in a quantum diffusive transport regime involves weak localization (WL) correction to the conductivity. WL/WAL originates due to the constructive/destructive quantum interference between self-intersecting paths of the fermions in a disordered system. In the case of a TI, WAL stems from the π Berry phase associated with massless Dirac fermions and leads to the enhancement of conductivity. On the contrary, there will be a decrement in conductivity for massive Dirac fermions, known as WL. In TI, topological surface electrons described by the gapless Dirac spectrum should yield a WAL-like feature, that is, a monotonic increase in 2D conductivity with a lowering of the temperature in a logarithmic scale. This observation is in stark contrast to the WL-like feature in the $G_S - \ln T$ plot observed in our experiments. This ambiguity is solved by Lu *et al.* pioneering the Lu-Shen model, stating that the $\ln T$ -dependence conductance is dominated by the stronger electron-electron interaction (EEI) over the WAL correction term [33]. At low temperatures, the total contribution to 2D conductance (ΔG_S) is expressed as

$$\Delta G_S(T) = G_S(T) - G_S(T_0) = \Delta G_{EEI}(T) + \Delta G_{qi}(T), \quad (1)$$

where T_0 indicates the reference temperature below which the $\ln T$ dependence of conductance starts, and ΔG_{EEI} and ΔG_{qi} are the contributions to the conductance corrections from EEI and quantum interference (qi) terms, respectively. Now, the $\ln T$ -dependence behavior can be quantitatively described by the *slope* extracted from the $G_S - \ln T$ plot, denoted by κ , which is as follows:

$$\kappa = \left(\frac{\pi h}{e^2} \right) \frac{\partial G_S}{\partial (\ln T)}. \quad (2)$$

One can write the total slope κ as $\kappa = \kappa_{EEI} + \kappa_{qi}$. κ_{EEI} is expressed as $\kappa_{EEI} = 1 - \eta_H F$, where F ($0 < F < 1$) is the Coulomb screening factor, suggested to be dependent on the permittivity of the material under study, and η_H lies between $3/4$ and 1 for $0 < \Delta_g/2E_F < 1$. Here, Δ_g denotes the mass gap, and E_F is the position of the Fermi level. On the other hand, $\kappa_{qi} = \alpha p$, where α is the prefactor extracted by fitting the out-of-plane magneto-conductivity data employing the Hikami-Larkin-Nagaoka equation [41,42], and p is the exponent extracted from the T dependence of the phase coherence length: $L_\phi \propto T^{-p/2}$. In other terms, α and p directly represent the quantum interference (qi) properties of each single coherent transport channel. For example, in the massless limit ($\Delta_g/2E_F = 0$), $\alpha = -1/2$ [42,43], $\eta_H = 3/4$ [33], and the expression for the sheet conductivity can be expressed as

$$\begin{aligned} G_S(T) &= \kappa \frac{e^2}{\pi h} \ln \left(\frac{T}{T_0} \right) + G_S(T_0) \\ &= \left(\alpha p + 1 - \frac{3}{4} F \right) \frac{e^2}{\pi h} \ln \left(\frac{T}{T_0} \right) + G_S(T_0). \end{aligned} \quad (3)$$

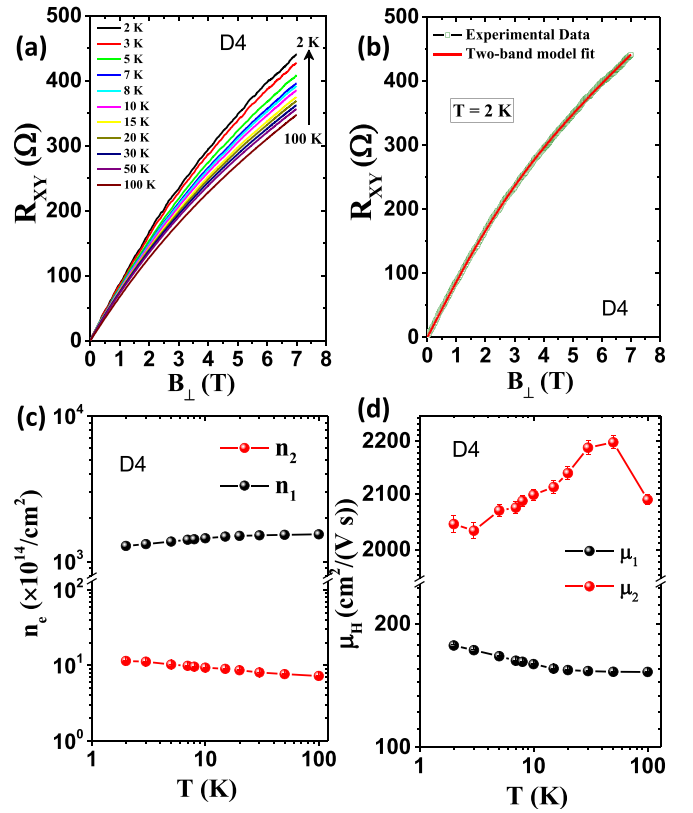


FIG. 2. Non-linear Hall effect. (a) All nonlinear Hall resistances as a function of applied magnetic fields for the device D4. (b) Fit to the Hall data acquired at 2 K according to the two-band model [Eq. (4)]. All the extracted (c) carrier densities and (d) mobilities at different temperatures are plotted.

In BSTS, since the relative permittivity ϵ_r is large as ~ 100 , the screening factor $F < 0.1$ and hence, the slope κ is always positive in the absence of a magnetic field. The positive value of κ is evident in our experiments.

B. Electrical transport at varying magnetic field

1. Hall effect

In order to determine the nature of the charge carriers in TI, we performed Hall measurements in the presence of a magnetic field applied normal to the sample. For three out of four devices, a linear fit to the Hall curves yields a negative charge carrier with carrier concentration $\sim 10^{13} - 10^{14} / \text{cm}^2$ and mobility of $\sim 130 - 180 \text{ cm}^2 / (\text{V s})$. The remaining device (D4: [BSTS(105 nm)/RuCl₃(20 nm)] shows nonlinearity in the Hall curve, as shown in Fig. 2(a), indicating the presence of two kinds of negative charge carriers with different mobility. To analyze the nonlinear Hall effect, we used the two-band model with the following formalism:

$$R_{XY} = \frac{B}{e} \frac{(n_1 \mu_1^2 + n_2 \mu_2^2) + (n_1 + n_2)(\mu_1 \mu_2 B)^2}{(|n_1| \mu_1 + |n_2| \mu_2)^2 + (n_1 + n_2)^2 (\mu_1 \mu_2 B)^2} \quad (4)$$

with constraint equation: $G_{XX}(B = 0) = e(n_1 \mu_1 + n_2 \mu_2)$. Here (n_1, μ_1) and (n_2, μ_2) is the 2D carrier concentrations

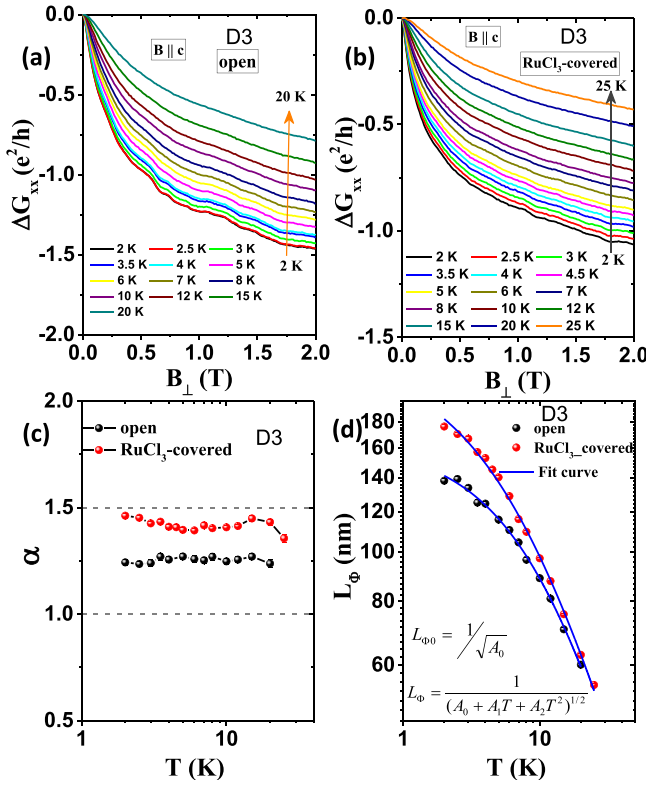


FIG. 3. Out-of-plane magnetoconductivity. (a), (b) Out-of-plane magnetoconductivity (MC) for the open and RuCl₃-covered region, respectively. (c) The prefactor α and (d) L_ϕ as a function of temperature. The Neel transitions (T_N) are indicated. [The ripples in MC in (a) are due to the universal conductance fluctuations (UCF), which is not the focus of this work.]

and mobilities, respectively, for two different carriers of the same sign, and e is the electronic charge and B , the applied magnetic field. Figure 2(b) displays the nonlinear Hall curve fitted with Eq. (4). Figures 2(c) and 2(d) depicts the plots of carrier concentrations and mobilities, respectively, as a function of temperature. These observations are in line with the findings in Ref. [31], where two different values of mobility were attributed to the two types of carriers related to (i) TSS and (ii) RSS. In our case, we obtained the same order in the values of mobility [~ 2000 and ~ 200 cm²/(V s)]. The lower mobility corresponds to topological surface carriers, while the higher mobility can be attributed to carriers associated with RSS. These observations are also consistent with the obtained value of α .

2. Multichannel weak antilocalization analysis

The magnetoresistance of a pristine 3D TI shows the sharp cusp feature in the presence of a small magnetic field normal to the sample surface, attributed to the WAL effect [1]. WAL behavior originates from the topological surface carriers, described as massless Dirac fermions, carrying π Berry phase. Conversely, bulk charge carriers can lead to WL, thus contributing to the positive magnetoconductance [44]. However, according to the Rashba model, Rashba surface states also carry π Berry phase, thus leading to the WAL effect [13]. Figure 3 displays the magneto-conductance data for the regions of BSTS flake: (i) open and (ii) RuCl₃-covered. In order to analyze the magneto-conductance data with the WAL feature, we have used Hikami-Larkin-Nagaoka (HLN) formalism which states that, in the quantum diffusive regime of a strong spin-orbit coupled system, the magnetoconductance has the following form [41]:

$$\Delta G_{XX}(B) = \alpha \frac{e^2}{\pi h} \left[\Psi \left(\frac{1}{2} + \frac{\hbar}{4eL_\phi^2 B} \right) - \ln \left(\frac{\hbar}{4eL_\phi^2 B} \right) \right], \quad (5)$$

where α and L_ϕ are the prefactor and the phase-coherence length, respectively, and $\Psi(x)$ denotes the digamma function. The leading fitting parameter α has to be corrected by multiplying with a suitable device aspect ratio $(L/W)_{\text{eff}}$ to obtain the correct number of uncoupled coherent transport channels, each contributing $\alpha = 0.5$ (see the Supplemental Material [34] for details). These conducting channels are spin-orbit coupled channels and preserve spin-momentum locking.

We fitted the sharp cusp of low-field magneto-conductance (WAL) data using the above-mentioned HLN equation [Eq. (5)] until 0.5 T. With increasing temperature, the WAL effect diminishes due to increasing channel decoherence. The corrected fitting parameter α ranges from 1 to 1.5 for all the devices (see Table I) while varying temperatures until 25 K. Since the values of α are close to 1.5, we can assume there are three spin-orbit coupled coherent transport channels: top and bottom TSS and electrically coupled Rashba surface states (RSS) [31,32].

As evident in Fig. 3(d), the phase coherence length L_ϕ follows a monotonic decreasing trend with increasing temperature, gradually destroying the WAL effect associated with carrier dephasing. During dephasing, the charge carrier undergoes inelastic collision, thus yielding to an additional phase that eventually destroys its quantum coherence. In 2D electronic systems, carrier dephasing mainly occurs by small-energy scale losses due to electron-electron interactions in the low-temperature regime, called the Nyquist dephasing mechanism where $L_\phi \propto T^{-1/2}$. At higher temperatures, the

TABLE I. Transport parameters for perpendicular fields.

Device	Thickness of BSTS flake	Thickness of RuCl ₃ flake	α at 2 K		$\Delta\kappa(B)$	
			open	RuCl ₃ -covered	open	RuCl ₃ -covered
D1	20 nm	35 nm		1.10		+1.0
D2	56 nm	63 nm		1.11		+1.0
D3	92 nm	100 nm	1.25	1.45	+1.0	+1.5
D4	105 nm	20 nm	1.30	1.30	+1.0	+1.0

dephasing mechanism is dominated by electron-phonon interaction $L_\phi \propto T^{-1}$ due to the creation of acoustic phonons that interacts with electrons. In our analysis, we have used the combined form to fit the $L_\phi - T$ plot:

$$L_\phi = \frac{1}{(A_0 + A_1 T + A_2 T^2)^{1/2}}, \quad (6)$$

where A_0 , A_1 , and A_2 are the fitting parameters and $A_0 = \frac{1}{L_{\phi 0}^2}$, takes care of the saturation in L_ϕ near 0 K. Here, $L_{\phi 0}$ is the phase coherence length at 0 K. The reason for this saturated L_ϕ is still debatable [45]. Figure 3(d) shows the comparison of the fitted plot in the case of open and RuCl_3 -covered regions of BSTS flake. It can be argued that the difference in L_ϕ for both regions is due to the degree of cleanliness of the BSTS flake. In the RuCl_3 -covered BSTS device, we notice no observable change in $\alpha - T$ and $L_\phi - T$ curves while crossing the antiferromagnetic transition temperatures (8 K and 15 K) of RuCl_3 , as shown in Fig. 3 [46]. The maximum net magnetic moment in RuCl_3 flake could have an apparent effect on the surface transport of BSTS. However, we think the obtained data are insufficient to conclude, and this observation needs to be corroborated by more detailed experiments.

C. Logarithmic T -dependence of sheet conductance at constant out-of-plane magnetic field

At low enough temperatures, we observed linear, logarithmic temperature dependence of sheet conductance, reminiscent of strong 2D electron-electron interaction in a quantum diffusive regime (Fig. 4). In this regard, we applied the Lu-Shen theory discussed before [33].

The slope κ in Eq. (3) has two parts: κ_{EEI} and κ_{qi} . Now since the quantum interference correction to the conductivity vanishes at high fields, $B \gg B_\phi$ where B_ϕ is the phase coherence field expressed as $B_\phi = \frac{\hbar}{4eL_\phi^2}$, κ_{qi} also vanishes. Note that L_ϕ is extracted from the perpendicular field transport data. On the contrary, κ_{EEI} is constant irrespective of the magnetic field. These two observations yield simpler expressions for two regimes of magnetic field range:

$$\kappa(B \ll B_\phi) = \alpha p + 1 - \frac{3}{4}F, \quad (7)$$

$$\kappa(B \gg B_\phi) = 1 - \frac{3}{4}F. \quad (8)$$

Therefore, at strong fields perpendicular to the sample, $\Delta\kappa(B = \infty) = \kappa(B = \infty) - \kappa(B = 0) = \kappa(B \gg B_\phi) - \kappa(B \ll B_\phi) \approx -\alpha p$. For instance, in the case of a single intact TSS channel, $\alpha = -1/2$ and $p = 1$ due to 2D electron-electron interaction dominant in the system ($L_\phi \propto T^{-p/2}$), $\Delta\kappa = +0.5$. This change in κ can be explained in terms of the Berry phase in the Dirac model as follows:

$$\phi_b = \pi \left(1 - \frac{\Delta_g}{2E_F} \right), \quad (9)$$

where Δ_g is the energy gap in the gapped Dirac surface states and E_F is the position of the Fermi level. One expects $\Delta\kappa = +0.5$ in the case of π Berry phase, which is the case of gapless surface states. For a gapped or massive Dirac system (for example, magnetically doped TI), $\Delta\kappa = -0.5$ due to the deviation of ϕ_b from π . Recently, Tkáč *et al.* have demonstrated how $\Delta\kappa$ is more sensitive to time-reversal breaking

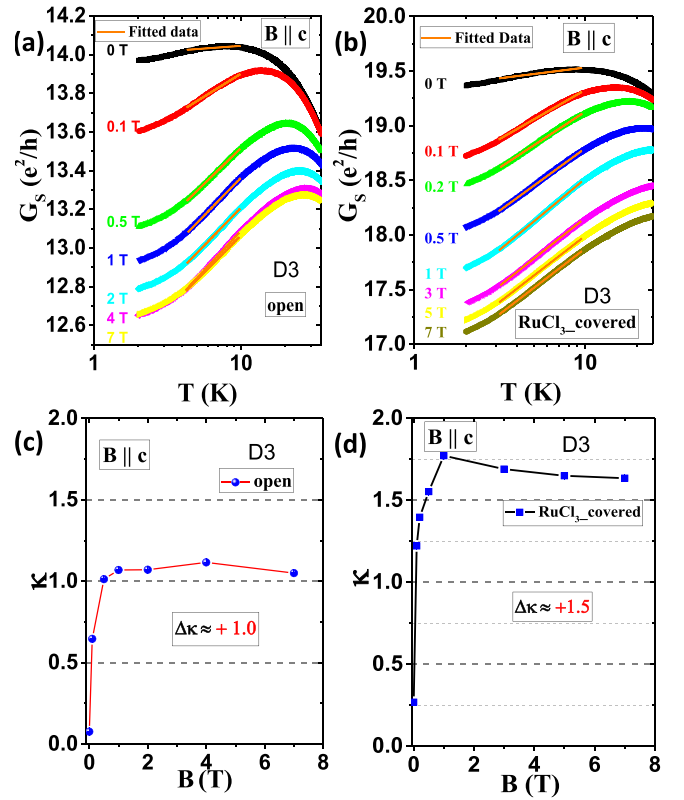


FIG. 4. Logarithmic temperature-dependent conductance at constant out-of-plane magnetic field. G_S - T semilogarithmic plot for devices D1, D2, and D4 at different out-of-plane fields and the corresponding change in the slope ($\Delta\kappa$) for (a), (b) the open region and (c), (d) the RuCl_3 covered region.

perturbations such as magnetic dopants in pristine TI in comparison to WAL that persists despite the change in π Berry phase (ϕ_b). Further, they have shown how $\Delta\kappa$ changes from $+0.5$ to -0.5 on crossing Curie transition temperature though the WAL behavior has been seen to manifest [47]. Previously there was evidence of WAL-WL crossover which requires magnetic doping to some extent in TI [48–51]. In this regard, the evaluation of $\Delta\kappa$ has been proved to be a more efficient tool to detect the minute change in the π Berry phase [47]. In other terms, it is more sensitive to the mass gap opening by magnetic doping in the gapless Dirac system such as TI, as discussed in Ref. [33]. Figures 4(a), 4(b) and 5(a), 5(c), 5(e), 5(f) display the $G_S - T$ semilogarithmic plot for magnetic fields applied perpendicular to the sample. On increasing field, the slope (κ) starts rising sharply and saturates soon, as evident in Figs. 4(c), 4(d) and 5(b), 5(d), 5(g). It turns out that $\Delta\kappa = +1.0$, twice the value of $+0.5$ associated with single TSS channel carrying π Berry phase, observed earlier in literature [37–40].

1. When $\Delta\kappa = +1.0$

In the case of open region, WAL measurement indicates the existence of top and bottom TSS and electrically coupled top and bottom RSS (Fig. 3). Therefore, we argue both TSS lead to $\Delta\kappa = (+0.5) + (+0.5)$, as evident in Figs. 4(c) and 5(b), 5(d), 5(g). However, the contribution in $\Delta\kappa$ from RSS

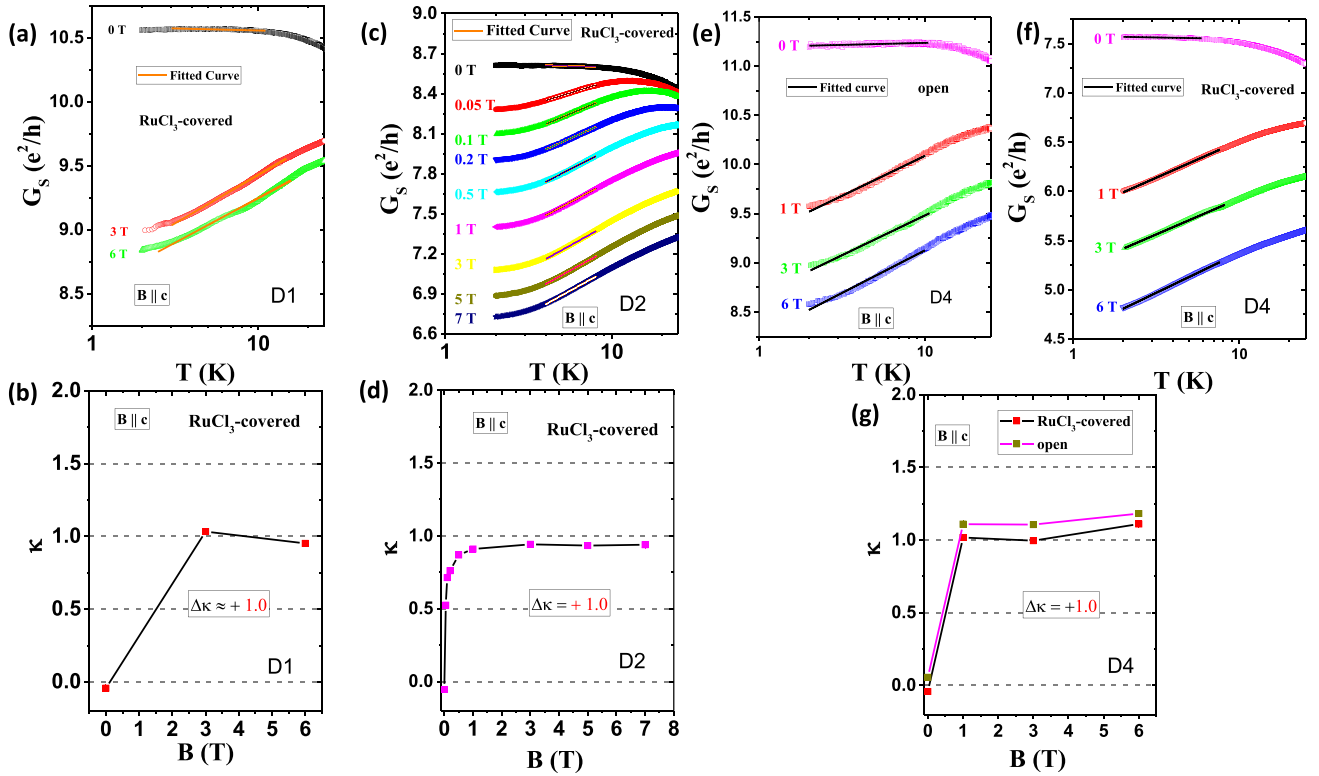


FIG. 5. Logarithmic temperature-dependent conductance at constant out-of-plane magnetic field. (a), (c), (e), (f) G_S - T semilogarithmic plot at different out-of-plane fields and (b), (d), (g) the corresponding change in the slope ($\Delta\kappa$) for the open region and the RuCl₃ covered region.

is not accounted for since the RSS are not only coupled with themselves but also interact with TSS via interband scattering (Fig. 6). Note that, though the intraband scattering for TSS is prohibited due to the absence of backscattering, the carriers are allowed to tunnel from TSS to the RSS bands, provided the tunneling rate is larger than the decoherence rate ($1/L_\phi^2$). This coupling between TSS and RSS is observed as the reduction in the value of α (~ 1.2) along with the small deviation from the π Berry phase in the case of RSS. This validates the observation of $\Delta\kappa = \Delta\kappa_{\text{top-TSS}} + \Delta\kappa_{\text{bottom-TSS}} = (+0.5) + (+0.5) = +1.0$ for three out of four devices (D1, D2, and D4) irrespective of coverage by RuCl₃ flake (Table I).

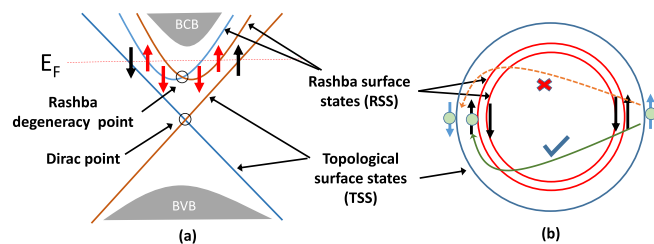


FIG. 6. Topological surface states (TSS) and Rashba surface states (RSS). (a) Schematic of band structures of a topological insulator. (b) Fermi circles for TSS and RSS along with the intra and interband scattering between TSS and RSS near the Fermi level. The former type of scattering is prohibited, while the latter type is allowed.

2. Evidence of Rashba surface states (RSS) coexisting with topological surface states (TSS) ($\Delta\kappa = +1.5$)

According to the Rashba model, Rashba fermions can also carry π Berry phase owing to the spin-momentum locking in a strongly spin-orbit coupled system such as TI [13]. Like TSS, RSS is also protected due to the time-reversal (TR) symmetry. Since Rashba spin-split surface states also give rise to gapless energy spectrum ($\Delta/2E_F = 0$), they can contribute to the $\ln T$ dependence of sheet conductance and can lead to $\Delta\kappa = +0.5$ according to the Lu-Shen theory [33].

During magnetotransport measurement of the hBN-encapsulated BSTS device, Abhishek *et al.* attributed the observed $\alpha = 2.0$ to the presence of top and bottom TSS and two decoupled top and bottom RSS by corroborating with ARPES measurements [6,31,32]. Two well-separated RSS (near the top and bottom surfaces) in the bulk-insulating TI arises from the band bending near the interfaces with hexagonal-BN and SiO₂. Moreover, TSS and RSS are physically well-separated from each other, and RSS resides deep inside the bulk while TSS forms on the surface where two insulators (here, hBN or SiO₂ or vacuum and BSTS) of topologically distinct classes meet. Abhishek *et al.* further argued that $\alpha = 1.5$ indicates the presence of top and bottom TSS as well as a coherent transport channel originating from the electrical coupling between top and bottom RSS. Therefore, our samples possess three single coherent conducting channels indicated by $\alpha \approx 1.5$ in the WAL measurements. We attribute the difference in the α and $\Delta\kappa$ of both regions of BSTS flake

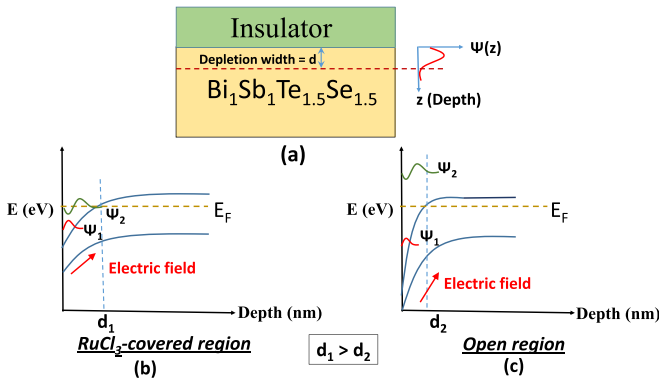


FIG. 7. Band bending in TI-nonTI interface. (a) A typical TI-nonTI interface where BSTS is TI and SiO_2 , vacuum, or RuCl_3 is the non-TI. (b), (c) Band bending with triangular potential well wherein Rashba states subbands reside for RuCl_3 -covered and open region of TI, respectively.

(device D3) to the possible charge transfer mechanism due to RuCl_3 , discussed in the next section.

3. Charge transfer induced band bending

Due to the quantum confinement, the Rashba 2DEGs have many subbands spatially distributed within the triangular potential well (Fig. 7). The solutions to the wave functions of bulk electrons confined in that region can be approximated as Airy functions that describe the nonrelativistic particles trapped in a triangular potential well [52]. The energy gap between two successive subbands depends on the depth and width of the potential well. We expect a shallower potential well in the case of less strong band bending, while the stronger band bending leads to a deeper potential well with smaller spatial width. So, for example, the energy gap between the ground and first excited states or subbands is smaller in the case of weaker band bending, while sufficiently strong band bending forces the bulk charge carriers to accommodate in the ground state only, hence closer to the interface.

For three BSTS devices [20 nm (D1), 56 nm (D2), and 105 nm (D4) thick] covered by the RuCl_3 layer with varying thicknesses [35 nm (D1), 63 nm (D2), and 35 nm (D4), respectively], the change in slopes, $\Delta\kappa$ are constant to +1.0 (see Table I and Fig. 5). The positive unity possibly corresponds to decoupled top and bottom TSS, each contributing +0.5. However, we notice a change in the value of $\Delta\kappa$ during the conductance measurement across the 100 nm thick RuCl_3 -covered region of 92 nm thick BSTS flake (device D3 in Table I). As usual, $\Delta\kappa = +1.0$ for the open region of the latter device. On the contrary, the covered region yields $\Delta\kappa = +1.5$, greater by +0.5 than that for other devices. These findings insist we consider one more gapless surface state carrying π Berry phase. We attributed the extra (+0.5) to the decoupled top-RSS spatially well-separated from the top-TSS but electrically coupled with bottom-RSS (near SiO_2 surface). This observation is corroborated by extracting $\alpha = 1.45$, closer to 1.5 than that for other devices, as evident from Table I. This notion can be understood from the strength of band bending and corresponding potential well with different depth, width,

and shape depending upon interaction with the interfacial layer.

RuCl_3 layer, when strained, can cause charge (hole) transfer to the next layer interfaced with it, as evident in the case of graphene (monolayer)/ RuCl_3 heterostructure [25,27]. Similarly, we expect hole transfer from the RuCl_3 layer to the electron-rich BSTS surface layer. The holes doped in the TI surface layer will compensate the negative charge somewhat, and the effect will be seen as the reduction in the strength of band bending. In other terms, RuCl_3 proximitized to the TI layer will make the triangular potential well shallower. As discussed before, the quantum confinement of bulk electrons within a triangular potential well leads to the multiple Rashba spin-split surface subbands spatially separated from each other. In the case of the shallower triangular potential well, the spatial separation between subbands is less. In turn, some subbands are expected to intersect the Fermi level. On the contrary, one subband will be deep inside the potential well, and other subbands will not be available due to the large enough energy gap in the case of the vacuum-interfaced region of the TI flake. This phenomenon can be understood in terms of the depletion region formed near the interface, as shown in Fig. 7. At the end of the depletion region inside the TI, we expect the Rashba surface states to reside. In the vicinity of the vacuum-TI interface, the depletion region is narrow enough to cause RSS and TSS coupling together. On the other hand, the RuCl_3 -TI surface provides a wider depletion region inside the TI to accommodate RSS subbands decoupled from the TSS. Eventually, this charge transfer induced band bending gives extra (+0.5) to $\Delta\kappa$ due to gapless RSS that carries π Berry phase [33]. So, the total change in the slope in the logarithmic temperature dependence of sheet conductance due to the RuCl_3 -covered region can be expressed as

$$\begin{aligned}\Delta\kappa &= \Delta\kappa_{\text{top-TSS}} + \Delta\kappa_{\text{bottom-TSS}} + \Delta\kappa_{\text{RSS}} \\ &= (+0.5) + (+0.5) + (+0.5) \\ &= +1.5.\end{aligned}\quad (10)$$

To corroborate our speculation, we take into account the value of α extracted from the perpendicular field magnetotransport. For the open region, α is lesser than for the covered region though $1 < \alpha < 1.5$ in both cases. Hence, in this way, the RuCl_3 has a possible proximity effect on TI surface states.

IV. CONCLUSION

In conclusion, we probed the electrical transport signature in 3D TI BSTS nanoflakes proximitized to exfoliated RuCl_3 nanoflakes. Multichannel WAL analysis of low-field magnetoconductance yields the prefactor α that ascertains the presence of TSS and Rashba spin-split conducting states (RSS) originating from quantum-confined bulk charge carriers near the TI-nonTI interface. The nonlinear Hall effect indicates Rashba fermions are distinct from topological Dirac fermions which have low mobility. At low temperatures, resistivity upturn manifests as linear logarithmic temperature $\ln T$ dependence of sheet conductance, revealing the electron-electron interaction and quantum interference effect. Furthermore, application of the Lu-Shen model to $\ln T$ dependence of sheet conductance at various constant out-of-plane

magnetic fields yields the maximum change in slope, $\Delta\kappa = +1.0$ for the top and bottom TSS each contributing (+0.5). In the case of $\Delta\kappa = +1.5$, additional +0.5 indicates the presence of a conducting coherent channel due to RSS. We observed the difference in the values of $\Delta\kappa$ for the open and RuCl₃-covered region of BSTS flake in the case of 100 nm thick RuCl₃. We argue that RuCl₃ injects holes into the electron-rich TI surface layer and causes compensation of bulk charge carriers, leading to weaker band bending and decoupling of RSS from TSS as captured by the value of $\Delta\kappa = +1.5$. However, we did not observe this difference in $\Delta\kappa$ for other TI devices covered by RuCl₃ with lesser thicknesses (<100 nm). Our experiments suggest that there could be another possibility; by lowering the thickness of the BSTS

flake, by forming edge-contact geometry via encapsulating the TI nanoflakes with RuCl₃ flakes or by tuning carrier density using gatevoltages, the hole injection would be appreciable which may result in some observable change in the electrical transport properties.

ACKNOWLEDGMENTS

We thank Nirmal K. Sebastian, Gagan Rastogi, and Abhinab Mohapatra for insightful discussions. We acknowledge the funding support from the Ministry of Education, Government of India. We thank the Micro-and-Nano characterization facility and the National Nano fabrication facility at CeNSE, IISc. We thank the AFMM facility in IISc.

-
- [1] M. Z. Hasan and C. L. Kane, Colloquium: Topological insulators, *Rev. Mod. Phys.* **82**, 3045 (2010).
- [2] Y. Chen, J. G. Analytis, J.-H. Chu, Z. Liu, S.-K. Mo, X.-L. Qi, H. Zhang, D. Lu, X. Dai, Z. Fang *et al.*, Experimental realization of a three-dimensional topological insulator, Bi₂Te₃, *Science* **325**, 178 (2009).
- [3] D. Hsieh, D. Qian, L. Wray, Y. Xia, Y. S. Hor, R. J. Cava, and M. Z. Hasan, A topological Dirac insulator in a quantum spin Hall phase, *Nature (London)* **452**, 970 (2008).
- [4] D. Hsieh, Y. Xia, D. Qian, L. Wray, F. Meier, J. H. Dil, J. Osterwalder, L. Patthey, A. V. Fedorov, H. Lin, A. Bansil, D. Grauer, Y. S. Hor, R. J. Cava, and M. Z. Hasan, Observation of Time-Reversal-Protected Single-Dirac-Cone Topological-Insulator States in Bi₂Te₃ and Sb₂Te₃, *Phys. Rev. Lett.* **103**, 146401 (2009).
- [5] Y. Ando, Topological insulator materials, *J. Phys. Soc. Jpn.* **82**, 102001 (2013).
- [6] H. Lohani, P. Mishra, A. Banerjee, K. Majhi, R. Ganesan, U. Manju, D. Topwal, P. S. A. Kumar, and B. R. Sekhar, Band structure of topological insulator BiSbTe_{1.25}Se_{1.75}, *Sci. Rep.* **7**, 4567 (2017).
- [7] Z. Ren, A. A. Taskin, S. Sasaki, K. Segawa, and Y. Ando, Large bulk resistivity and surface quantum oscillations in the topological insulator Bi₂Te₂Se, *Phys. Rev. B* **82**, 241306(R) (2010).
- [8] Z. Ren, A. A. Taskin, S. Sasaki, K. Segawa, and Y. Ando, Optimizing Bi_{2-x}Sb_xTe_{3-y}Se_y solid solutions to approach the intrinsic topological insulator regime, *Phys. Rev. B* **84**, 165311 (2011).
- [9] T.-C. Hsiung, D.-Y. Chen, L. Zhao, Y.-H. Lin, C.-Y. Mou, T.-K. Lee, M.-K. Wu, and Y.-Y. Chen, Enhanced surface mobility and quantum oscillations in topological insulator Bi_{1.5}Sb_{0.5}Te_{1.7}Se_{1.3} nanoflakes, *Appl. Phys. Lett.* **103**, 163111 (2013).
- [10] Y. Xu, I. Miotkowski, C. Liu, J. Tian, H. Nam, N. Alidoust, J. Hu, C.-K. Shih, M. Z. Hasan, and Y. P. Chen, Observation of topological surface state quantum hall effect in an intrinsic three-dimensional topological insulator, *Nat. Phys.* **10**, 956 (2014).
- [11] B. Xia, P. Ren, A. Sulaev, P. Liu, S.-Q. Shen, and L. Wang, Indications of surface-dominated transport in single crystalline nanoflake devices of topological insulator Bi_{1.5}Sb_{0.5}Te_{1.8}Se_{1.2}, *Phys. Rev. B* **87**, 085442 (2013).
- [12] B. Skinner, T. Chen, and B. I. Shklovskii, Why Is the Bulk Resistivity of Topological Insulators So Small? *Phys. Rev. Lett.* **109**, 176801 (2012).
- [13] S.-Q. Shen, Spin hall effect and berry phase in two-dimensional electron gas, *Phys. Rev. B* **70**, 081311 (2004).
- [14] S. Trebst, Kitaev materials, *Phys. Rep.* **950**, 1 (2022).
- [15] A. Banerjee, C. Bridges, J.-Q. Yan, A. Aczel, L. Li, M. Stone, G. Granroth, M. Lumsden, Y. Yiu, J. Knolle *et al.*, Proximate kitaev quantum spin liquid behaviour in a honeycomb magnet, *Nat. Mater.* **15**, 733 (2016).
- [16] J. A. Sears, L. E. Chern, S. Kim, P. J. Bereciartua, S. Francoual, Y. B. Kim, and Y.-J. Kim, Ferromagnetic Kitaev interaction and the origin of large magnetic anisotropy in α -RuCl₃, *Nat. Phys.* **16**, 837 (2020).
- [17] K. W. Plumb, J. P. Clancy, L. J. Sandilands, V. V. Shankar, Y. F. Hu, K. S. Burch, H.-Y. Kee, and Y.-J. Kim, α -RuCl₃: A spin-orbit assisted Mott insulator on a honeycomb lattice, *Phys. Rev. B* **90**, 041112 (2014).
- [18] A. Koitzsch, C. Habenicht, E. Müller, M. Knupfer, B. Büchner, H. C. Kandpal, J. van den Brink, D. Nowak, A. Isaeva, and T. Doert, J_{eff} Description of the Honeycomb Mott Insulator α -RuCl₃, *Phys. Rev. Lett.* **117**, 126403 (2016).
- [19] L. Binotto, I. Pollini, and G. Spinolo, Optical and transport properties of the magnetic semiconductor α -RuCl₃, *Phys. Stat. Sol. (b)* **44**, 245 (1971).
- [20] A. Banerjee, J. Yan, J. Knolle, C. A. Bridges, M. B. Stone, M. D. Lumsden, D. G. Mandrus, D. A. Tennant, R. Moessner, and S. E. Nagler, Neutron scattering in the proximate quantum spin liquid α -RuCl₃, *Science* **356**, 1055 (2017).
- [21] Y. Kasahara, T. Ohnishi, Y. Mizukami, O. Tanaka, S. Ma, K. Sugii, N. Kurita, H. Tanaka, J. Nasu, Y. Motome *et al.*, Majorana quantization and half-integer thermal quantum Hall effect in a Kitaev spin liquid, *Nature (London)* **559**, 227 (2018).
- [22] O. Tanaka, Y. Mizukami, R. Harasawa, K. Hashimoto, K. Hwang, N. Kurita, H. Tanaka, S. Fujimoto, Y. Matsuda, E.-G. Moon *et al.*, Thermodynamic evidence for a field-angle-dependent Majorana gap in a Kitaev spin liquid, *Nat. Phys.* **18**, 429 (2022).
- [23] J. Bruin, R. Claus, Y. Matsumoto, N. Kurita, H. Tanaka, and H. Takagi, Robustness of the thermal Hall effect close to half-quantization in α -rucl3, *Nat. Phys.* **18**, 401 (2022).
- [24] A. Kitaev, Anyons in an exactly solved model and beyond, *Ann. Phys.* **321**, 2 (2006).

- [25] S. Biswas, Y. Li, S. M. Winter, J. Knolle, and R. Valentí, Electronic Properties of α -RuCl₃ in Proximity to Graphene, *Phys. Rev. Lett.* **123**, 237201 (2019).
- [26] S. Mashhadi, Y. Kim, J. Kim, D. Weber, T. Taniguchi, K. Watanabe, N. Park, B. Lotsch, J. H. Smet, M. Burghard *et al.*, Spin-split band hybridization in graphene proximitized with α -RuCl₃ nanosheets, *Nano Lett.* **19**, 4659 (2019).
- [27] B. Zhou, J. Balgley, P. Lampen-Kelley, J.-Q. Yan, D. G. Mandrus, and E. A. Henriksen, Evidence for charge transfer and proximate magnetism in graphene- α -RuCl₃ heterostructures, *Phys. Rev. B* **100**, 165426 (2019).
- [28] D. J. Rizzo, S. Shabani, B. S. Jessen, J. Zhang, A. S. McLeod, C. Rubio-Verdú, F. L. Ruta, M. Cothrine, J. Yan, D. G. Mandrus *et al.*, Nanometer-scale lateral p-n junctions in graphene/ α -RuCl₃ heterostructures, *Nano Lett.* **22**, 1946 (2022).
- [29] J. Pack, B. Jessen, S. Liu, J. Yan, K. Watanabe, T. Taniguchi, D. Mandrus, J. Hone, and C. Dean, Transport in WSe₂ proximitized to RuCl₃, *Bull. Am. Phys. Soc.* (2022), <https://meetings.aps.org/Meeting/MAR23/Session/D20.4>.
- [30] D. Kirk and M. Kuroda, Analysis of charge transfer doping in RuCl₃/semiconducting transition metal dichalcogenide heterostructures from first principles, *Bull. Am. Phys. Soc.* (2022), <https://meetings.aps.org/Meeting/MAR22/Session/K60.4>.
- [31] A. Banerjee, A. Sundaresh, K. Majhi, R. Ganesan, and P. S. Anil Kumar, Accessing rashba states in electrostatically gated topological insulator devices, *Appl. Phys. Lett.* **109**, 232408 (2016).
- [32] A. Banerjee, A. Sundaresh, R. Ganesan, and P. S. Anil Kumar, Spatially varying electronic dephasing in three-dimensional topological insulators, *Phys. Rev. B* **98**, 155423 (2018).
- [33] H.-Z. Lu and S.-Q. Shen, Finite-Temperature Conductivity and Magnetoconductivity of Topological Insulators, *Phys. Rev. Lett.* **112**, 146601 (2014).
- [34] See Supplemental Material at <http://link.aps.org/supplemental/10.1103/PhysRevB.107.245418> for the characterization of bulk Bi₁Sb₁Te_{1.5}Se_{1.5} and RuCl₃ single crystals; details of hot, dry transfer technique to prepare BSTS/RuCl₃ heterostructures; calculation of effective device aspect ratio; activated and variable range hopping transport of the bulk BSTS crystal; additional Hall and magneto-resistance data; analysis of in-plane magneto-transport; additional data on $\Delta\kappa$ for uncovered and covered region by α -RuCl₃; analysis of $\ln(T)$ -dependence sheet conductance data in presence of constant in-plane magnetic field; and it also includes Refs. [7,10–12,16,27,31,32].
- [35] J. Wang, A. M. DaSilva, C.-Z. Chang, K. He, J. K. Jain, N. Samarth, X.-C. Ma, Q.-K. Xue, and M. H. Chan, Evidence for electron-electron interaction in topological insulator thin films, *Phys. Rev. B* **83**, 245438 (2011).
- [36] M. Liu, C.-Z. Chang, Z. Zhang, Y. Zhang, W. Ruan, K. He, L.-L. Wang, X. Chen, J.-F. Jia, S.-C. Zhang, Q.-K. Xue, X. Ma, and Y. Wang, Electron interaction-driven insulating ground state in Bi₂Se₃ topological insulators in the two-dimensional limit, *Phys. Rev. B* **83**, 165440 (2011).
- [37] J. Chen, X. Y. He, K. H. Wu, Z. Q. Ji, L. Lu, J. R. Shi, J. H. Smet, and Y. Q. Li, Tunable surface conductivity in Bi₂Se₃ revealed in diffusive electron transport, *Phys. Rev. B* **83**, 241304 (2011).
- [38] Y. Takagaki, B. Jenichen, U. Jahn, M. Ramsteiner, and K.-J. Friedland, Weak antilocalization and electron-electron interaction effects in cu-doped Bi₂Se₃ films, *Phys. Rev. B* **85**, 115314 (2012).
- [39] S.-P. Chiu and J.-J. Lin, Weak antilocalization in topological insulator Bi₂Te₃ microflakes, *Phys. Rev. B* **87**, 035122 (2013).
- [40] A. Roy, S. Guchhait, S. Sonde, R. Dey, T. Pramanik, A. Rai, H. C. Movva, L. Colombo, and S. K. Banerjee, Two-dimensional weak anti-localization in Bi₂Te₃ thin film grown on si (111)-(7×7) surface by molecular beam epitaxy, *Appl. Phys. Lett.* **102**, 163118 (2013).
- [41] S. Hikami, A. I. Larkin, and Y. Nagaoka, Spin-orbit interaction and magnetoresistance in the two dimensional random system, *Prog. Theor. Phys.* **63**, 707 (1980).
- [42] H.-Z. Lu, J. Shi, and S.-Q. Shen, Competition between Weak Localization and Antilocalization in Topological Surface States, *Phys. Rev. Lett.* **107**, 076801 (2011).
- [43] G. Tkachov and E. M. Hankiewicz, Weak antilocalization in hgte quantum wells and topological surface states: Massive versus massless dirac fermions, *Phys. Rev. B* **84**, 035444 (2011).
- [44] H.-Z. Lu and S.-Q. Shen, Weak localization of bulk channels in topological insulator thin films, *Phys. Rev. B* **84**, 125138 (2011).
- [45] S. Islam, S. Bhattacharyya, H. Nhalil, M. Banerjee, A. Richardella, A. Kandala, D. Sen, N. Samarth, S. Elizabeth, and A. Ghosh, Low-temperature saturation of phase coherence length in topological insulators, *Phys. Rev. B* **99**, 245407 (2019).
- [46] J. A. Sears, M. Songvilay, K. W. Plumb, J. P. Clancy, Y. Qiu, Y. Zhao, D. Parshall, and Y.-J. Kim, Magnetic order in α -RuCl₃: A honeycomb-lattice quantum magnet with strong spin-orbit coupling, *Phys. Rev. B* **91**, 144420 (2015).
- [47] V. Tkáč, K. Výborný, V. Komanický, J. Warmuth, M. Michiardi, A. S. Nganku, M. Vondráček, R. Tarasenko, M. Vališka, V. Stetsovych, K. Carva, I. Garate, M. Bianchi, J. Wiebe, V. Holy, P. Hofmann, G. Springholz, V. Sechovsky, and J. Honolka, Influence of an Anomalous Temperature Dependence of the Phase Coherence Length on the Conductivity of Magnetic Topological Insulators, *Phys. Rev. Lett.* **123**, 036406 (2019).
- [48] D. Zhang, A. Richardella, D. W. Rench, S.-Y. Xu, A. Kandala, T. C. Flanagan, H. Beidenkopf, A. L. Yeats, B. B. Buckley, P. V. Klimov *et al.*, Interplay between ferromagnetism, surface states, and quantum corrections in a magnetically doped topological insulator, *Phys. Rev. B* **86**, 205127 (2012).
- [49] L. Bao, W. Wang, N. Meyer, Y. Liu, C. Zhang, K. Wang, P. Ai, and F. Xiu, Quantum corrections crossover and ferromagnetism in magnetic topological insulators, *Sci. Rep.* **3**, 2391 (2013).
- [50] C.-Z. Chang, P. Tang, Y.-L. Wang, X. Feng, K. Li, Z. Zhang, Y. Wang, L.-L. Wang, X. Chen, C. Liu *et al.*, Chemical-Potential-Dependent Gap Opening at the Dirac Surface States of Bi₂Se₃ Induced by Aggregated Substitutional Cr Atoms, *Phys. Rev. Lett.* **112**, 056801 (2014).
- [51] M. Liu, J. Zhang, C.-Z. Chang, Z. Zhang, X. Feng, K. Li, K. He, L.-L. Wang, X. Chen, X. Dai *et al.*, Crossover between Weak Antilocalization and Weak Localization in a Magnetically Doped Topological Insulator, *Phys. Rev. Lett.* **108**, 036805 (2012).
- [52] J. H. Davies, *The Physics of Low-Dimensional Semiconductors: An Introduction* (Cambridge University Press, 1998).